Stability Analysis of Localized States and Deterministic Single Soliton Generation in a Kerr Microresonator Under Thermo-Optic Nonlinear Effects

Qinglin Fang, Haojie Xia, *Member, IEEE*, Mingjie Jiao, Feifan Xu, and Xueying Jin

***Abstract*—Thermal effects are ubiquitous in high-quality resonators and microcomb-based high precision measurements. We present a stability analysis of the thermodynamics in a driven Kerr microresonator theoretically and numerically, using the thermal Lugiato-Lefever model. We analyze the spatial bifurcation structure and existence range of stationary states depending on the thermal parameters. Our study shows that, the thermal effect causes the original bifurcation structure to change from Hamiltonian-Hopf bifurcation to Belyakov-Devaney bifurcation. In addition, a stability map of various stationary regions in the parameter space of cavity detuning and the pump power is achieved through numerical simulations of thermal Lugiato–Lefever equation, and we propose a deterministic route to obtain the stable cavity soliton state avoiding the chaotic and unstable regions under the influence of thermal effects. Our approach has potential value for obtaining stable solitary Kerr comb sources under practical conditions.**

***Index Terms*—Dynamics process, optical frequency comb, thermal effects, stable soliton.**

I. Introduction

KERR frequency comb is a set of equidistant spectral components generated by optically pumping whispering gallery mode (WGM) resonators with high quality factors and Kerr nonlinearity. The spacing between adjacent combs is determined by the free spectrum range (FSR) of the microresonator In addition, as the Kerr frequency combs exhibit high coherence, high repetition rate, and small size easy to package, they provide a powerful tool for broad application prospects, such as precision frequency /distance measurement [1], [2], [3], astronomical spectroscopic calibration [4], arbitrary waveform generation [5], radio frequency/microwave signal sources [6], and multi-wavelength light sources for coherent optical communication [7], [8].

In the research field of optical frequency combs based on micro-nano resonators, there are currently two mainstream theoretical models for describing the dynamic evolution of the optical field. One is the coupled mode equations [9], which describe the coupling relationships between different modes inside the resonator from a frequency domain perspective. The other is the Lugiato-Lefever Equation (LLE) [10], which describes the envelope evolution of the optical field from a time domain perspective. However, the LLE can reduce the computational complexity by several orders of magnitude, greatly improving simulation efficiency.

To describe the nonlinear dynamics of light in the microresonator cavity, in the mean field approximation, such a cavity can be modelled using the well-known Lugiato-Lefever (LL) equation. Currently, most of previous research works have been devoted to the investigation of the dynamics in microresonators under anomalous dispersion and normal dispersion [11], [12]. Based on this, the steady state and stability characteristics of Turing patterns, periodic patterns, and soliton crystals have been well understood [13], [14], [15], [16], [17], [18], [19]. However, most theoretical progress has overlooked the role of thermal effects on the waveform and stability of the optical field within the microresonator cavity. The thermal effect will cause the resonance frequency of the cavity to shift. Under the influence of thermal effects, when the pump light is in an effective blue detuned state, the effective resonance frequency can be locked. However, when the pump light is in an effective red detuned state, the frequency cannot be locked, making it difficult for soliton states to operate in a stable regime. So far, the generation of solitons has been demonstrated in microresonators, including forward and backward pumped laser scanning [20], [21], pump power modulation [22], etc. However, directly and deterministically generating and maintaining a single soliton state in a microresonator remains a challenge. Although many articles have proposed explicit and systematic theories and approaches to reach the soliton regime, and these methods include chaos-avoiding trajectory [23], [24], [25], single-pulse triggering [26], sudden detuning setting [27], [28], or slow pump modulation

Manuscript received 30 November 2023; revised 6 February 2024; accepted 22 February 2024. Date of publication 27 February 2024; date of current version 7 March 2024. This work was supported in part by the National Natural Science Foundation of China (NSFC) under Grant 52375534 and Grant 62005071, in part by the National Key Research and Development Program of China under Grant 2019YFE010747, in part by Anhui Provincial Science and Technique Program under Grant 202003a05020008, and in part by the Fundamental Research Funds for the Central Universities under Grant JZ2021HGTB0079. *(Corresponding author: Xueying Jin.)*

The authors are with the Anhui Province Key Laboratory of Measuring Theory and Precision Instrument, School of Instrument Science and Optoelectronics Engineering, Hefei University of Technology, Hefei 230009, China (e-mail: qlfang@mail.hfut.edu.cn; hjxia@hfut.edu.cn; jiaomj@mail.hfut.edu.cn; 2021110003@mail.hfut.edu.cn; xyjin007@hfut.edu.cn).

Digital Object Identifier 10.1109/JPHOT.2024.3370179

[29], [30]. Nevertheless, there is a lack of comprehensive research concerning the deterministic generation of solitons in the presence of thermal effects. Additionally, the nonlinear dynamic processes are not analyzed in detail after the inclusion of thermal effects, and the available data is insufficient from existing theories. Further research on the influence of thermal effects on soliton formation, especially the nonlinear dynamic processes and the formation process of deterministic solitons, is particularly interesting.

In this article, we investigate the stability and thermo-optical dynamics of Kerr resonators theoretically and numerically [31]. By analyzing the Lugiato-Lefever (LL) equation, the basic properties and the cubic equation for optical bistability of its steady-state solutions are given, and the uniform steady-state characteristics and their linear stability in the main mode of the system are studied accordingly. It is found that modulation instability affects both the upper and lower branches of the bistable equation solution in the absence of thermal effects, while in the presence of thermal effects, modulation instability affects the upper branch of the solution. This is because the spatial branching has changed under the influence of thermal effects. Therefore, a spatial bifurcation analysis is performed for the system and different equilibrium states of the equation are classified. Additionally, we found that under typical thermal conditions, the lower branch is less susceptible to modulation instability, and thus the deterministic access path of the soliton must start from a relatively small detuning. Finally, we propose a deterministic path that can access the stable cavity soliton (SCS) region avoiding the unstable chaotic regions in the presence of thermal instability. Our results provide important insights into soliton dynamics involving thermal effects.

II. Thermo-Optical Equations of Motion

In order to describe the dynamics of the intracavity field, we adopted a spatiotemporal LL formalism by including the terms induced by thermal effects [32]. After performing a normalization process from the Ref. [32], the corresponding equation is the following partial differential equation:

$$\frac{\partial \psi}{\partial t} = -\left[1 + i\left(\alpha + \theta\right)\right]\psi + \frac{i}{2}\frac{\partial^2 \psi}{\partial x^2} + i|\psi|^2\psi + F,$$
$$\psi(x = 0,\ t) = \psi(x = L,\ t) \tag{1}$$

$$\frac{d\theta}{dt} = -AP - B\theta, \tag{2}$$

where

$$P = \int_0^L |\psi|^2 \frac{dx}{L}. \tag{3}$$

ψ represents the complex envelope of the entire intracavity field, x is the position along the propagation direction of the resonator with $0 \leq x \leq L$, L is the cavity length, t is the dimensionless time, α refers to the detuning between the pump light field and the resonant wavelength of the cold cavity, θ denotes the thermal detuning, F is the pump intensity. While A is the conversion coefficient of the thermal detuning, B is the thermal relaxation coefficient of the resonator [21], the parameters A and B are usually small, 10^{-1} or smaller, but the thermal sensitivity ratio C = A/B can be smaller or larger, meaning that the thermal effect is moderate or strong. P represents the mean power. All the parameters in the normalized LL equation are dimensionless, which allows for numerical calculations without being restricted to specific resonator parameters, and is beneficial for analyzing the general laws of Kerr frequency comb evolution.

III. Study on Dynamic Process of Optical Frequency Comb

A. Steady-State Solutions and Their Stability

To find various equilibrium points of the system and determine their stability, we start by setting $\partial\psi/\partial t = 0$, such that the envelope $\psi_s(x)$ is independent of time. And the heat dissipation is given by

$$\theta_S = -CP_s, \tag{4}$$

where P_s is the average power and $C = A/B$ is the thermal sensitivity parameter. As mentioned above, $\psi_s(x)$ follows the equation

$$-\left[1 + i\left(\alpha - CP_s\right)\right]\psi_s + \frac{i}{2}\frac{\partial^2 \psi_s}{\partial x^2} + i|\psi_s|^2\psi_s + F = 0, \tag{5}$$

By setting $\partial^2\psi/\partial x^2 = 0$, one can obtain equilibrium solutions of the optical-field equation solution $\psi_s(x) = \psi_c$ for (5), the average power can be expressed as $|\psi_c|^2$. Therefore, the thermal nonlinearity can be combined with the Kerr nonlinearity following

$$-\left(1 + i\alpha\right)\psi_c + i\left(1 + C\right)|\psi_c|^2\psi_c + F = 0, \tag{6}$$

Solution ψ_c can then be expressed as

$$\psi_c = U_C + iV_C, U_C = \frac{F}{1 + \left(\left(1 + C\right)I_h - \alpha\right)^2},$$
$$V_c = \frac{\left(\left(1 + C\right)I_h - \alpha\right)F}{1 + \left(\left(1 + C\right)I_h - \alpha\right)^2}, \tag{7}$$

where $I_h \equiv |\psi_c|^2$ satisfies the classical cubic equation of optical bistability

$$\left(1 + C\right)^2 {I_h}^3 - 2\left(1 + C\right)\alpha {I_h}^2 + \left(1 + \alpha^2\right)I_h = F^2$$
$$= H\left(\alpha, I_h\right), \tag{8}$$

$I_h \equiv |\psi_c|^2$indicates the equilibrium cavity field intensity. Equation (8) is a cubic equation with respect to I_h, and the number of solutions depends on the values of F and α. To determine the structure of $H(\alpha, I_h)$, we find the extreme points with respect to I_h:

$$\frac{\partial H}{\partial I_h} = 3(1 + C)^2 {I_h}^2 - 4\alpha\left(1 + C\right)I_h + \alpha^2 + 1, \tag{9}$$

the discriminant of the quadratic equation above is $\Delta = 4(1 + C)^2(\alpha^2 - 3)$, and thus when $\alpha < \sqrt{3}$, (8) is monotonic with only one solution and I_h is single-valued. When $\alpha > \sqrt{3}$, I_h has three values. In the latter case, a pair of saddle-node

bifurcations $SN_{b,t}$ occurs at

$$I_{b,t}\ (\alpha) = |\varphi_{b,t}|^2\ = \frac{2\alpha \pm \sqrt{\alpha^2 - 3}}{3\,(1+C)}, \tag{10}$$

the corresponding pumping term is given as

$$F_{\pm}^2\ (\alpha) = \frac{2\alpha \mp \sqrt{\alpha^2-3}}{3\,(1+C)}\ \left(1 + \left(\frac{\sqrt{\alpha^2-3} \pm \alpha}{3}\right)^2\right). \tag{11}$$

To determine the stability of the steady-state solution, we introduce the perturbations $\psi\ = \psi_s\ + \psi_1$ and $\theta\ = -CP_s + \theta_1$, where ψ_1 and θ_1 are small perturbation quantities. By substituting ψ and θ into the LL equation and neglecting higher-order terms, we obtain

$$\begin{aligned}\frac{\partial \psi_1}{\partial t}\ =\ & -\left[1 + i\,(\alpha - CP_s)\right]\psi_1 - i\theta_1\psi_s + \frac{i}{2}\frac{\partial^2\psi_1}{\partial x^2} \\ & + 2i|\psi_s|^2\psi_1 + i{\psi_s}^2{\psi_1}^*,\end{aligned} \tag{12}$$

$$\frac{d\theta_1}{dt} =\ -AP_1 - B\theta_1, \tag{13}$$

due to translational invariance, the (12) has solutions of the form $\psi_1\ (x,t) = \psi_{k+}\ (t)e^{ikx} + \psi_{k-}(t)e^{-ikx}$, for uniform $\psi_s \equiv \psi_c$. And with $k \neq 0,\ P_1 =\ 0$, we have $\theta_1 =\ 0$. Therefore, the equation can be presented as

$$\begin{aligned}\frac{\partial \psi_1}{\partial t}\ =\ & -\left[1 + i\,(\alpha - CP_S)\right]\psi_1 + \frac{i}{2}\frac{\partial^2\psi_1}{\partial x^2} + 2i|\psi_c|^2\psi_1 \\ & + i{\psi_c}^2{\psi_1}^*\end{aligned} \tag{14}$$

substituting $\psi_1(x,t)$ into (14) and through its complex conjugate equation, we give the characteristic equation for the perturbation

$$\frac{\partial}{\partial t}\begin{bmatrix}\psi_{k+}\\ \psi_{k-}\end{bmatrix} = (-1 + iM)\begin{pmatrix}\psi_{k+}\\ \psi_{k-}\end{pmatrix}, \tag{15}$$

$$M\ = \begin{bmatrix}-\left(\alpha + \frac{1}{2}K^2 - (2+C)\,|\psi_c|^2\right) & {\psi_c}^2 \\ -(\psi_c^*)^2 & \alpha + \frac{1}{2}K^2 - (2+C)\,|\psi_c|^2\end{bmatrix} \tag{16}$$

where $*$ represents complex conjugation. Since $I_h \equiv |\psi_c|^2$, the expression of the eigenvalue equation of the above matrix is

$$\lambda^2 + \left[\alpha + \frac{1}{2}k^2 - (2+C)\,I_h\right]^2 -\ {I_h}^2 =\ 0, \tag{17}$$

and its eigenvalue solution is given by [33]

$$\lambda\ =\ \pm\sqrt{{I_h}^2 - \left[\alpha + \frac{1.}{2}k^2 - (2+C)\,I_h\right]^2}, \tag{18}$$

therefore, when $\lambda > 1$, new frequency comb lines will be generated and amplified through four-wave mixing, breaking the steady state of the cavity field. Thus, the non-steady state condition of the cavity field can be obtained through (18) as

$$W\ \left(k^2\right) = \frac{1}{4}\,k^4 + \left[(2+C)\,I_h - \alpha\right]k^2 + \left[(2+C)^2 - 1\right]{I_h}^2$$

$$-\,2\alpha\,(2+C)\,I_h + \alpha^2 + 1 < 0. \tag{19}$$

The left side of the equation is a quadratic function with respect to k^2. For the (19) to hold, the following conditions must be satisfied

1) Discriminant $\Delta > 0$, meaning $\Delta = {\mathrm{I_h}}^2 - 1 > 0$.
2) The right root of $\mathrm{W}\ (\mathrm{k}^2) =\ 0$ is greater than zero, which means $2[(2+C)I_h - \alpha] + \sqrt{{I_h}^2 - 1} > 0$.

With the above two conditions, the non-steady state condition can be described with the consideration of thermal effects and anomalous dispersion:

$$\begin{cases} I_h > 1\ , \alpha < 2 + C \\ I_h > \frac{(2+C)\alpha - \sqrt{\alpha^2 - (2+C)^2 + 1}}{(2+C)^2 - 1}.\ \alpha > 2 + C \end{cases} \tag{20}$$

In the non-steady state regime, the optical frequency comb will be generated from noise through four-wave mixing and form a certain distribution in the time domain. Therefore, studying the dynamics of the optical frequency comb in the non-steady state regime is of great significance.

B. Spatial Bifurcation Analysis

Spatial bifurcation analysis is the study of the structure and stability of steady-state solutions of a dynamic system based on the variation of parameters [34]. By bifurcation analysis, the existence region information of specific static solutions in parametric space can be obtained. In the modified LL equation, by setting the time derivative term $\frac{\partial \psi}{\partial t} =\ 0$, and separating the intracavity field into $\psi\ = \psi_r\ + i\psi_i$, where ψ_r is the real part of ψ and ψ_i is the imaginary part of ψ, the original (1) can be expressed as:

$$\frac{\partial^2\psi_r}{\partial x^2} =\ -2\left\{\psi_r\left[{\psi_r}^2 + {\psi_i}^2 - (\alpha - CP_s)\right] - \psi_i\right\}, \tag{21}$$

$$\frac{\partial^2\psi_i}{\partial x^2} =\ -2\left\{\psi_i\left[{\psi_r}^2 + {\psi_i}^2 - (\alpha - CP_s)\right] + \psi_r - F\right\}, \tag{22}$$

At this point, we introduce an intermediate variable

$$\emptyset_{r,i} = \frac{\partial \psi_{r,i}}{\partial x}, \tag{23}$$

and substitute it into the previous two equations, obtaining

$$\frac{\partial \psi_r}{\partial x} = \emptyset_r, \tag{24}$$

$$\frac{\partial \emptyset_r}{\partial x} =\ -2\left\{\psi_r\left[{\psi_r}^2 + {\psi_i}^2 - (\alpha - CP_s)\right] - \psi_i\right\}, \tag{25}$$

$$\frac{\partial \psi_i}{\partial x} = \emptyset_i, \tag{26}$$

$$\frac{\partial \emptyset_i}{\partial x} =\ -2\left\{\psi_i\left[{\psi_r}^2 + {\psi_i}^2 - (\alpha - CP_s)\right] + \psi_r - F\right\}, \tag{27}$$

In order to find possible forms of steady-state solutions, the linearized characteristic equation $\psi_c = \psi_{c,r}\ + i\psi_{c,i}$ is obtained around the equilibrium state shown at the bottom of the next page.

Through calculation, it can be obtained that the eigenvalues of the above characteristic equation follow the condition

$$\lambda^4 + 4\lambda^2\left(2\left(1+C\right)I_h - \alpha\right) + 4\left[3(1+C)^2{I_h}^2 - 4\alpha\left(1+C\right)I_h + \alpha^2 + 1\right] = 0, \quad (29)$$

Note that the eigenvalue equation is a quadratic equation as regard to λ^2, and thus for each equilibrium state I_h, it corresponds to four eigenvalues, such that these eigenvalues appear in pairs that are either opposite (λ^2 being real) or conjugate pairs (λ^2 being complex). In the $\alpha - F^2$ parameter space, if $\alpha < \sqrt{3}$ or $\alpha > \sqrt{3}$, and $F^2 < F_-^2(\alpha)$ and $F^2 > F_+^2(\alpha)$, each F^2 corresponds to four eigenvalues; if $\alpha > \sqrt{3}$ and $F_-^2(\alpha) < F^2 < F_+^2(\alpha)$, each F^2corresponds to twelve eigenvalues; and if $F^2 = F_-^2(\alpha)$ or $F^2 = F_+^2(\alpha)$, each F^2 corresponds to eight eigenvalues. Since the discriminant of the characteristic equation is $\Delta = 16[(1+C)^2{I_h}^2 - 1]$, the relationship between I_h and 1/(1+C) determines the style of the eigenvalues λ.

We next analyze the form of the eigenvalues λ in three cases: $I_h > 1/1 + C$, $I_h = 1/1 + C$, and $I_h < 1/1 + C$. When $I_h > 1/1 + C$, for discriminant $\Delta > 0$, there are two real roots for the eigenvalues

$$\lambda^2 = 2\left[\alpha - 2\left(1+C\right)I_h \pm \sqrt{(1+C)^2{I_h}^2 - 1}\right], \quad (30)$$

by analyzing the above formula, it is seen that the sign of λ^2 depends on the relationship between $|\alpha - 2(1+C)I_h|$ and $\sqrt{(1+C)^2{I_h}^2 - 1}$. Here we define the function

$$G\left(\alpha, I_h\right) = \left(\alpha - 2\left(1+C\right)I_h\right)^2 - \sqrt{(1+C)^2{I_h}^2 - 1}^2 = 4\left[3(1+C)^2{I_h}^2 - 4\alpha\left(1+C\right)I_h + \alpha^2 + 1\right]. \quad (31)$$

1) If $G(\alpha, I_h) > 0$, then the eigenvalue λ takes the following form: if $\alpha - 2(1+C)I_h > 0, (\lambda_{1,2}; \lambda_{3,4}) = (\pm a; \pm b)$. In this case, if $\alpha - 2(1+C)I_h = 0, (\lambda_{1,2}; \lambda_{3,4}) = (0; 0)$; and if $\alpha - 2(1+C)I_h < 0, (\lambda_{1,2}; \lambda_{3,4}) = (\pm ia; \pm ib)$;
2) If $G(\alpha, I_h) = 0$, the eigenvalue λ takes the following form: if $\alpha - 2(1+C)I_h > 0, (\lambda_{1,2}; \lambda_{3,4}) = (\pm a; 0)$. Thus, if$\alpha - 2(1+C)I_h = 0, (\lambda_{1,2}; \lambda_{3,4}) = (0; 0)$; if $\alpha - 2(1+C)I_h < 0, (\lambda_{1,2}; \lambda_{3,4}) = (0; \pm ib)$;
3) If $G(\alpha, I_h) < 0$, the eigenvalue λ takes the following form: $(\lambda_{1,2}; \lambda_{3,4}) = (\pm a; \pm ib)$.

When $I_h = 1/1 + C$, the discriminant $\Delta = 0$, and in this case, the eigenvalue λ has two identical real roots

$$\lambda^2 = 2\left(\alpha - 2\right), \quad (32)$$

the eigenvalue λ takes the following form if $\alpha > 2, (\lambda_{1,2}; \lambda_{3,4}) = (\pm a\,; \pm a)$; if $\alpha = 2, (\lambda_{1,2}\,; \lambda_{3,4}) = (0; 0)$; if $< 2, (\lambda_{1,2}\,; \lambda_{3,4}) = (\pm ia; \pm ia)$.

When $I_h < 1/1 + C$, the discriminant $\Delta < 0$, and in this case, the eigenvalue λ has two complex roots

$$\lambda^2 = 2\left[\alpha - 2\left(1+C\right)I_h \pm i\sqrt{(1+C)^2{I_h}^2 - 1}\right], \quad (33)$$

the eigenvalue λ takes the following form: $(\lambda_{1,2}; \lambda_{3,4}) = (a \pm ib; a \pm ib)$.

Fig. 1 shows the spatial characteristic values configuration corresponding to each segment of the curve (different colors). Takens-Bogdanov (RTB) bifurcation occurs when the eigenvalues consist of a pair of 0 and a pair of purely real numbers. In the vicinity of this bifurcation line, periodic and localized solutions can stably exist. Takens-Bogdanov-Hopf (RTBH) bifurcation emerges when the eigenvalues consist of a pair of zero and a pair of purely imaginary numbers. In the vicinity of this bifurcation line, only periodic and quasiperiodic solutions can stably exist. While the quadruple-zero (QZ) bifurcation rises when the eigenvalues have two pairs of zeros, and thus it is also commonly referred to as the "quadruple-zero" bifurcation. Various dynamics can be observed around it. Fig. 1(b) shows the stability variation of ψ_c when the thermal parameter $C = 0$, indicating no thermal effect. It can be seen that the lower branch of the solution is initially stable, but becomes unstable after undergoing a HH bifurcation due to modulation instability. Compared to Fig. 1(b) and (c) represents the stability of the solution branch under the same detuning when the thermal parameter *C* does not exceed its threshold. It is observed that when the thermal effect is weak, the stability of the solution branch and its corresponding bifurcation structure are the same as those without thermal effect. Fig. 1(d) represents the stability change of the lower branch of the solution when the thermal parameter *C* exceeds a certain threshold, indicating a relatively strong thermal effect. In this case, the stability of the lower branch of the solution changes, and some unstable regions without thermal effect become stable. Additionally, the HH bifurcation and the boundary between the middle and lower branches change to BD bifurcation and RTB bifurcation, respectively. Fig. 1(e) and (f) represent the further increase in detuning and thermal parameter, respectively, and the corresponding changes in the stability of the solution and bifurcation structure. At this point, the lower branch remains stable, indicating that the modulation instability does not affect the lower branch. Therefore, it can be observed from Fig. 1 that, in the vicinity of the thermal parameter threshold, the stability of the solution and bifurcation structure will change with the thermal parameter *C*, yet once the thermal effect exceeds the threshold, the bifurcation structure becomes stable and insensitive to the thermal parameter.

$$J = \begin{bmatrix} 0 & 1 & 0 & 0 \\ -2[3(1+C)\psi_{c,r}^2 + (1+C)\psi_{c,i}^2 - \alpha] & 0 & -2[2(1+C)\psi_{c,r}\psi_{c,i} - 1] & 0 \\ 0 & 0 & 0 & 1 \\ -2[2(1+C)\psi_{c,r}\psi_{c,i} + 1] & 0 & -2[(1+C)\psi_{c,r}^2 + 3(1+C)\psi_{c,i}^2 - \alpha] & 0 \end{bmatrix} \quad (28)$$

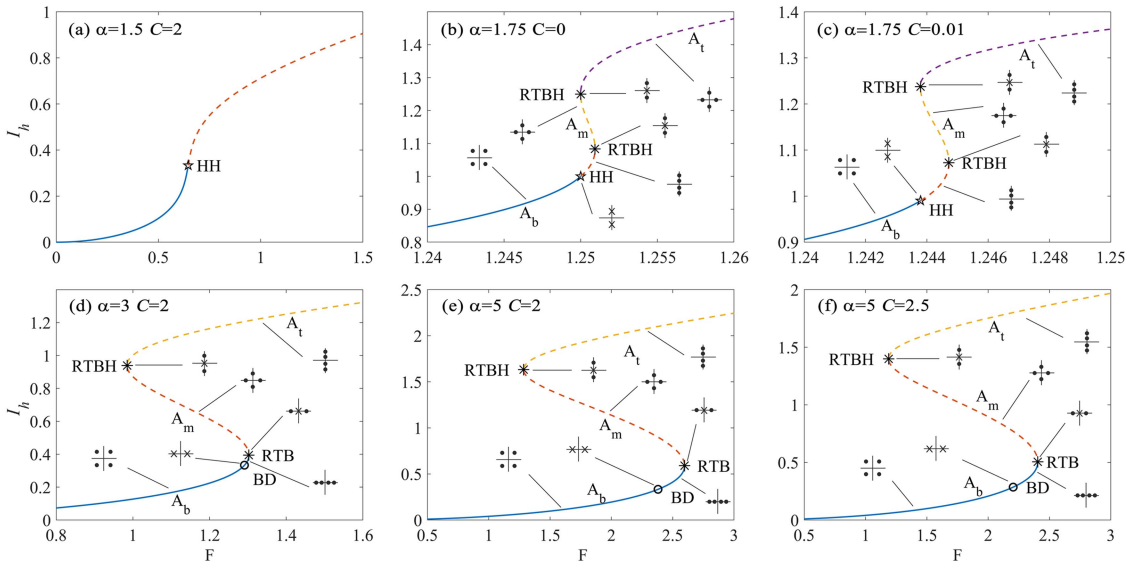

Fig. 1. Homogeneous steady states and steady-state diagrams for different detunings and thermal parameters under anomalous dispersion. (a) $\alpha = 1.5$, $C = 2$; (b)$\alpha = 1.75$, $C = 0$; (c)$\alpha = 1.75$, $C = 0.01$; (d)$\alpha = 3$, $C = 2$; (e)$\alpha = 5$, $C = 2$; (f)$\alpha = 5$, $C = 2.5$. Solid lines represent stable states while dashed lines represent unstable states. The four different bifurcations, namely HH, BD, RTB, and RTBH, are denoted by different symbols. HH bifurcation points are represented by the blank star (☆), BD bifurcation points by the blank circle, and RTB and RTBH bifurcation points by the asterisk. The different pictorial representations display the corresponding spatial eigenvalue configurations that describe the spatial stability. A_t , A_m and A_b represent the three branches of the solution.

TABLE I
EIGENVALUES AND REVERSIBLE SPATIAL BIFURCATIONS IN THE THERMAL LUGIATO-LEFEVER MODEL

Type	Nomenclature	Eigenvalue($\lambda_{1,2}$; $\lambda_{3,4}$)	pictogram	Location in Fig.2
1		$(\pm a; \pm b)$		
2	QZ	$(0; 0)$		b
3		$(\pm ia; \pm ib)$		
4	RTB	$(\pm a; 0)$		B_2
5	RTBH	$(0; \pm ib)$		B_2,C_1,C_2,b,c
6		$(\pm a; \pm ib)$		
7	HH	$(\pm ia; \pm ia)$		A_1,A_2
8	BD	$(\pm a; \pm a)$		A_3
9		$(a \pm ib; a \pm ib)$		

The Spatial bifurcation analysis developed in section B allows us to obtain bifurcation diagram (Fig. 2) under anomalous dispersion, including thermal effects. Table I shows the nomenclature and pictograph of the various eigenvalue sets. Each equilibrium has a set of four eigenvalues, and some classified bifurcations are attached to certain configurations of the eigenvalues. As can be seen in Fig. 2, although there exist four identical bifurcation structures in the diagram, the eigenvalue structures are different from the case in Ref. [35]. This difference indicates that some bifurcation structures in the bistable diagram will change under the influence of thermal effects. Compared to previous work [35], in the absence of thermal effects, line A1 in Fig. 2 corresponds to the Hamiltonian-Hopf (HH) bifurcation, which actually corresponds to modulation instability and leads to the generation of Turing patterns. HH bifurcation occurs when the eigenvalues consist of a pair of purely imaginary numbers. Near this bifurcation, solutions include quasiperiodic, periodic, and localized solutions [36]. However, after the inclusion of thermal effects, this bifurcation becomes the Belyakov-Devaney (BD) bifurcation, and modulation instability does not exist. BD bifurcation takes place when the eigenvalues consist of a pair of purely real numbers. Near the BD bifurcation line, Turing loop formations cannot be generated. However, there is one exception, which is when the thermal sensitivity parameter C

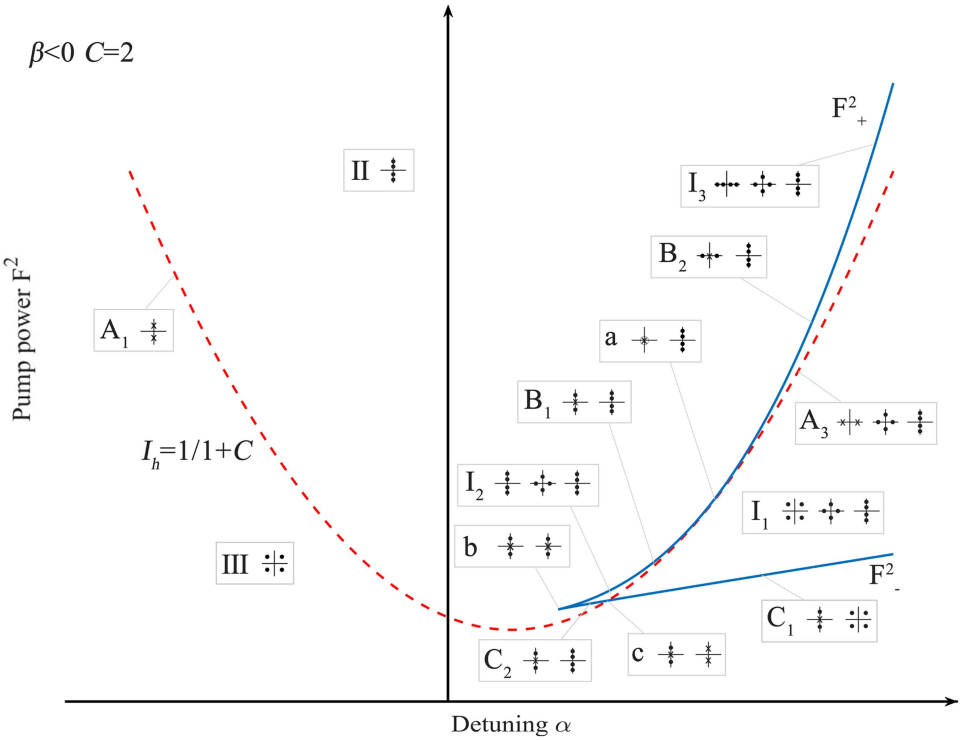

Fig. 2. Bifurcation diagram of the eigenvalue with the consideration of thermal effects under anomalous dispersion (not in proportion). The regions separated by colored lines are labeled with Roman numerals I, II, III. The colored lines are represented by capital letters: The red dashed line represents the bistable curve at $I_h = 1/1+C$, denoted as line A, which is further divided into segments A1, A2, A3. The blue solid line represents line B, C, which is further divided into segments B1, B2, C1, C2. The intersections of these colored lines are denoted by lowercase letters (a), (b), (c). In regions II and III, the system has only one equilibrium, while in region I, there are three equilibria. On the blue solid line, there are two equilibria. Therefore, in regions II and III, there is only one set of spatial eigenvalues (one eigenvalue bifurcation diagram), while region I corresponds to three sets of spatial eigenvalues (three eigenvalue bifurcation diagrams). On the blue solid line, there are two sets of spatial eigenvalues (two eigenvalue bifurcation diagrams).

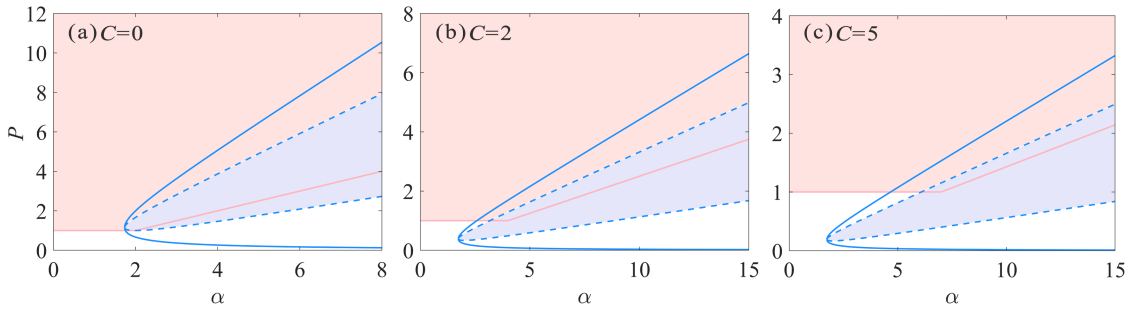

Fig. 3. Influence of modulation instability on the bifurcation of the bistable solution is shown in the α-P plane considering the thermal effect. Each point on the α-P plane uniquely corresponds to a continuous wave (CW) solution. The solid blue line delineates the boundary of the region with three solutions at the same pump power, and the dashed blue line distinguishes the branch boundaries. The red-brown area signifies modulational instability, while the blue area marks intermediate branches that are unreachable. (a)–(c) represent the graphs for the thermal sensitivity parameters $C = 0$, $C = 2$, and $C = 5$, respectively.

$= 0.15$ is relatively small. In this case, the influence of thermal effects is not significant and the HH bifurcation still exists, indicating the presence of modulation instability. Therefore, from a more general perspective, under typical thermal conditions, the lower branch is not easily affected by modulation instability. Therefore, the deterministic access path of solitons must start from a relatively small detuning, which will be reflected in the formation of deterministic single solitons in Section IV.

To gain more insight into the influence of modulation instability under thermal effect on the branch of bistable solution, the bifurcation diagram is depicted in $\alpha - P$ parameter plane with distinct thermal parameters, as shown in Fig. 3. According to (8), it is shown that $I_h = |\psi_c|^2$ follows a cubic (12), with all real solutions being positive and mapping to unique (8) complex solutions. Therefore, for any set parameter, one or three continuous wave (CW) solutions exist. When a thermal sensitivity ratio C = 2, which correspond to Fig. 2, a wedge-shaped coexistence region for three CW solutions appears in the parameter space of $\alpha - F^2$. As C increases, the region of coexistence will move downward, so for any thermal parameter C, the region of coexistence is a wedge-shaped domain with boundaries. Unlike the parameterization with $\alpha - F^2$, for functions of a and P,

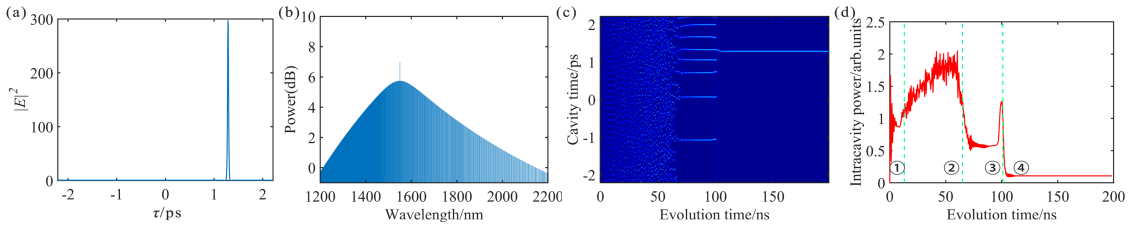

Fig. 4. Evolution of soliton and Kerr optical frequency comb in a microcavity, when corrections from thermal effects are taken into account. (a) Temporal waveform of the optical soliton; (b) frequency spectrum of the optical soliton; (c) evolution process of the Kerr optical frequency comb; (d) power variation in the evolution process of the optical frequency comb, where ①, ②, ③, ④ represent the four stages of comb evolution.

each a and P pairing in Fig. 3 corresponds to a specific CW solution, making it possible to track specific CW solutions to study the continuous wave solutions in the $\alpha - F^2$ parameter space. Here, three CW branches are demarcated within the blue solid line boundary, with transitions indicated by blue dashed lines. Thus, solutions below, between, and above these dashed lines pertain to lower, middle, and upper branches. Similarly, as C increases, the coexistence region in the α-P plane also decreases.

As can be seen in Fig. 3(a), for $\alpha < 2 + C$, modulation instability can simultaneously affect both the lower and upper branches. On this regard, the modulation instability boundary curve intersects with the coexistence region below its tip, making the lower branch a modulational instability one (Fig. 3(a)), which is the case when thermal effects are not considered. Based on our spatial bifurcation analysis shown in Fig. 1(b), the bifurcations in the corresponding bistable diagram are HH and RTBH bifurcations in this situation. However, with the increasing of thermal sensitivity parameter C, the coexistence region moves downward. When the thermal parameter C exceeds a certain threshold, the tip of the coexistence region, where the continuous wave branch meets, crosses the modulation instability boundary. At this point, modulation instability only affects the upper branch (Fig. 3(b)). When C has not reached its threshold, the bifurcations in the corresponding bistable diagram (Fig. 1(c)) are the same as those without thermal effects ($C = 0$), which are HH and RTBH bifurcations. Nevertheless, with C exceeding its threshold, the bifurcations in the corresponding bistable diagram (Fig. 1(d)) are BD, RTB, and RTBH bifurcations, that is to say, the bifurcation nature changes from HH bifurcation to BD bifurcation. Near the HH bifurcation, the equilibrium state becomes unstable under perturbation and modulation instability occurs, resulting in the formation of primary sidebands and Turing ring patterns in the time domain. However, near the BD bifurcation, modulation instability does not occur. For $\alpha > 2 + C$, considering that the middle branch is unreachable, modulation instability only affects the upper branch of the coexistence region (Fig. 3(c)). Therefore, from the perspective of spatial bifurcation, we believe that this is the fundamental reason why the coexistence region moves downward and modulation instability affects different branches as C increases. When C continues to increase, its spatial bifurcation does not change (Fig. 1(e), and (f)). In short, the thermal effect can affect the stability of the microcavity frequency comb, that is, under typical thermal conditions, the HH bifurcation in the bistable curve will transition to BD bifurcation, resulting in the disappearance of modulation instability.

IV. Deterministic SCS Generation

A. SCS Excitation With Thermal Effects

To demonstrate the effectiveness of the proposed theory, we performed a numerical calculation by desolving (1) using a two-step method. First, we calculate the effective detuning (laser detuning and thermal detuning) at each step, and then substitute it into the equation for numerical simulation. For simplicity, the simulation in this article did not take into account higher-order dispersion terms and other nonlinear effects (such as Raman, Self-steepening effect, High order dispersion) that exist in actual systems. Numerical simulation of the thermal LLE equation is performed using the split-step Fourier algorithm. By utilizing the simulated LLE with thermal effects correction, the evolution of Kerr comb spectrum and temporal waveform with respect to the pump detuning can be aquired [37]. Generally, with the forward detuning procedure, the full evolution of the intracavity field and optical spectrum can be divided into four stages: stable modulation instability (SMI), unstable modulation instability (UMI), unstable cavity soliton (UCS), and stable cavity soliton (SCS) [38], [39].

In the evolution process of Kerr combs, when pump is scanned from the blue-detuned to the red-detuned region, the intracavity field experiences four stages. In the first stage (SMI), the intracavity power increases rapidly, and modulation instability generates the main comb lines in its gain spectrum, and more secondary comb lines are generated through four-wave mixing. In the second stage (UMI), the intracavity power continues to increase, the overlapping of different secondary comb lines as well as quasi-dispersion compensation cause the phase mismatch between different frequency components, and thus the intracavity modes become chaotic in both frequency and time domains, leading to a low-coherence, high-noise modulation instability phase. In the third stage (UCS), the intracavity power decreases rapidly, and most of the gains obtained from random jitter cannot compensate for the cavity losses, gradually disappearing from the cavity. Finally, the intracavity power stabilizes, and one or more soliton can be stably created (SCS). Compared with the evolution process without considering the thermal effect, the power inside the cavity will suddenly increase in the evolution process from the third stage to the fourth stage, and then decrease to a stable state, which is different from the case without thermal

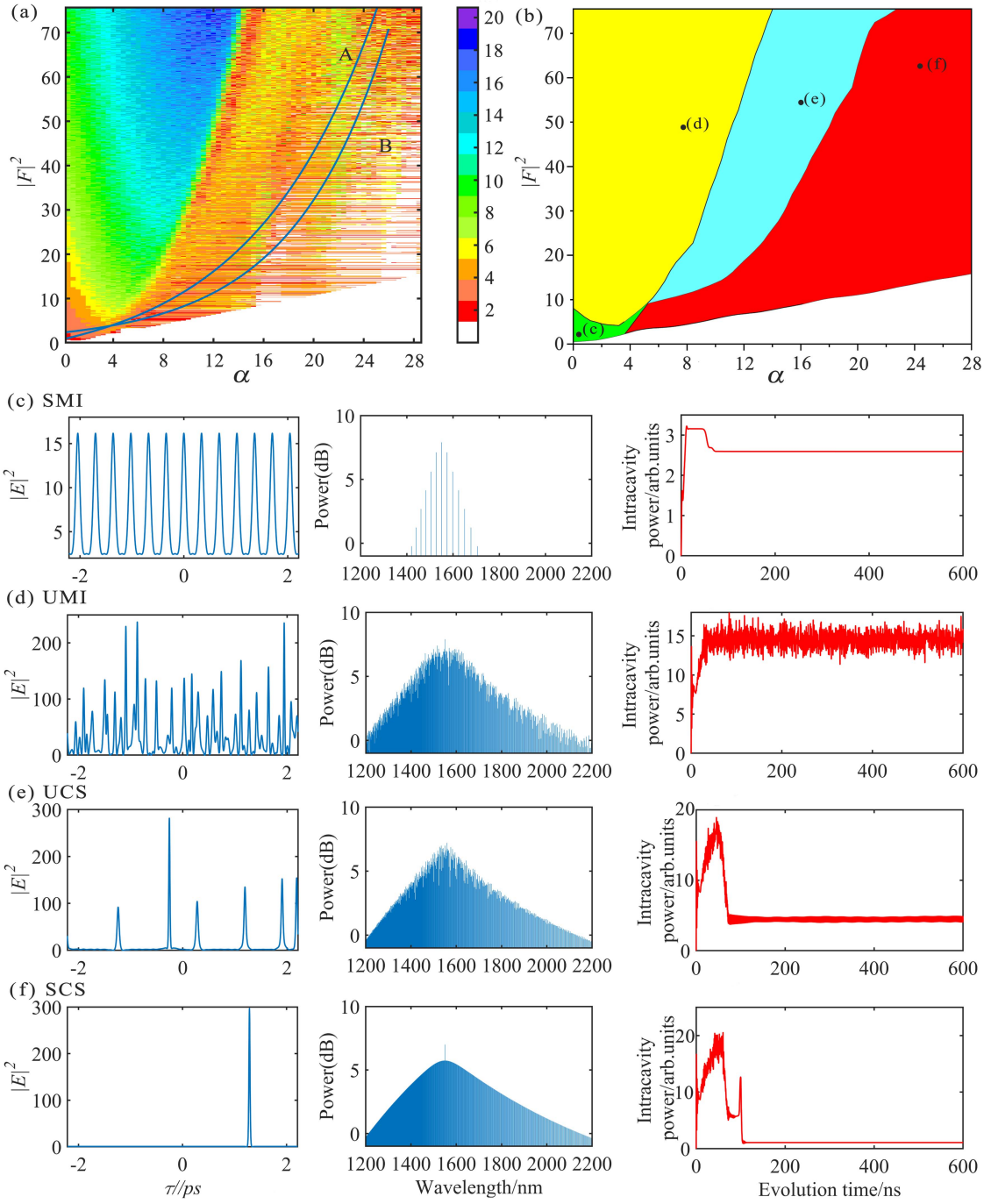

Fig. 5. (a) By traversing the simulation, obtain the distribution of different types of optical frequency combs in the parameter space $(\alpha, |F|^2)$. (b) Distribution map of Turing rings (green region), solitons (red region), unstable cavity solitons (blue region), and chaotic states (yellow region) in the parameter space of $(\alpha, |F|^2)$. (c)–(f) Four stages in the evolution of the optical frequency comb, with time-domain waveform (left), spectrum (middle), and the relationship between intra-cavity energy and time (right). (c) SMI region, (d) UMI region, (e) UCS region, (f) SCS region.

effect where the power decreases in a stepwise manner. In addition, according to our simulation results, the existence range of solitons ranges is defined from the minimum detuning of solitons generated to the maximum detuning of solitons disappeared. It should be noted that in the simulation, the initial field in the cavity is a weak Gaussian pulse, which is conducive to generating stable solitons. It is seen that when no thermal effect is added, the existence range of solitons ranges from 0.079 to 0.25; when thermal effect is added, the existence range of solitons ranges from 0.069 to 0.32. Therefore, the inclusion of thermal effects increases the range of soliton existence and enhances stability.

In order to present the existence domain of each state and their mutual relationships, we obtained the existence regions of various states of the optical frequency comb by traversing the simulation (Fig. 5(a)). However, it is difficult to determine

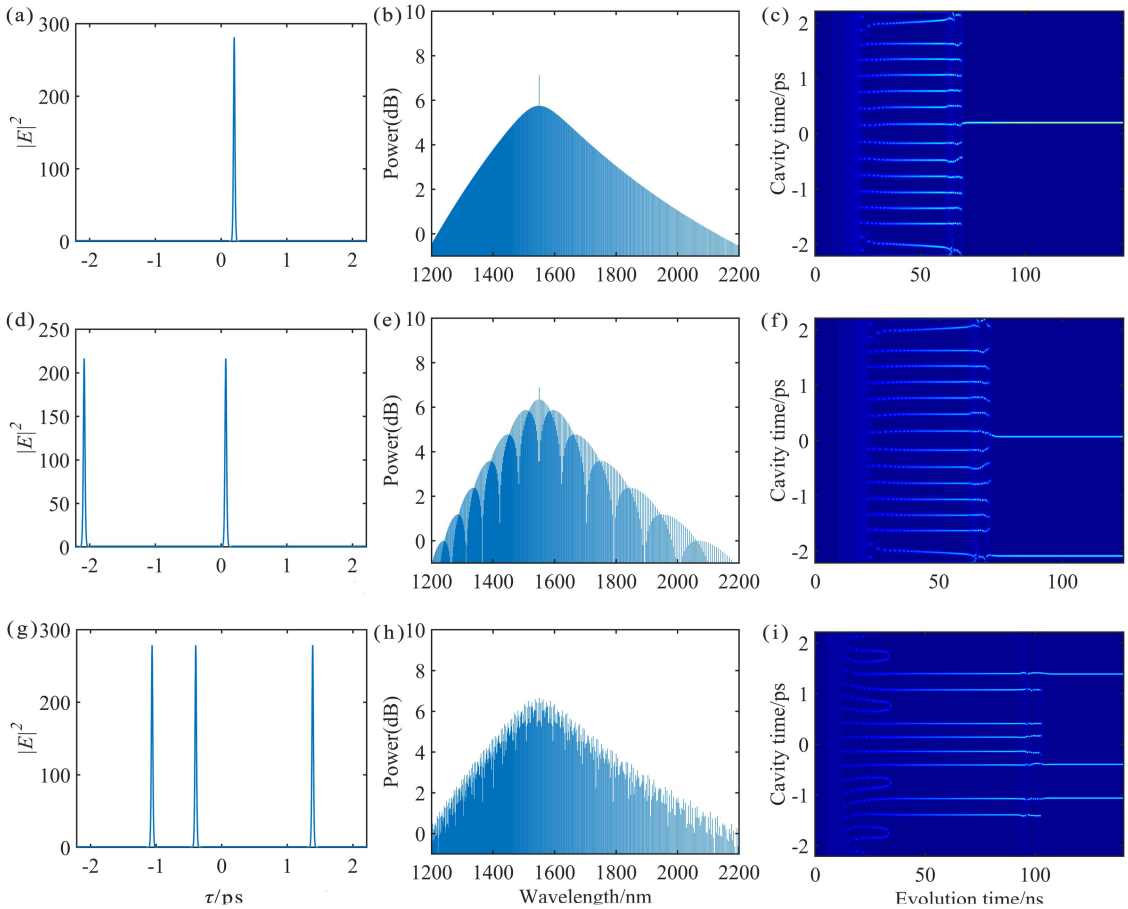

Fig. 6. Simulation results of avoiding chaotic state under different paths and different end points in the presence of thermal effects. (a)–(f) Represent simulation result figures of the same path with different endpoints, including soliton time-domain waveform (left), spectrum (middle), and soliton evolution (right). (a)–(c) Indicate the final result as a multi-soliton state optical comb. (d)–(f) Indicate the final result as a single-soliton state. (g)–(i) Represent soliton state optical combs obtained under different paths.

the boundary of the characteristic region for these states using theoretical equations. Nevertheless, the boundaries of each characteristic region can be determined based on the different characteristics of the optical frequency comb in terms of its temporal waveform, spectrum, and intra-cavity power evolution in the four stages of comb evolution. Fig. 5(b) shows the specific classification of each characteristic region, where the green region represents the stable stage of modulation instability (SMI), i.e., the Turing state; the yellow region represents the unstable stage of modulation instability (UMI), i.e., the chaotic state; the blue region represents the unstable stage of cavity solitons (UCS); and the red region represents the stable stage of cavity solitons (SCS). Fig. 5(c) to (f) respectively depict the characteristic plots of the Turing state, chaotic state, unstable cavity soliton state, and stable cavity soliton state, from which it can be seen that their temporal waveforms, spectra, and intra-cavity power curves are different. Then, on the parameter plane of $\alpha - |F|^2$, the existence domains of these states are obtained, which provides a foundation for deterministic soliton accessing paths in the following section. And our result confirms that the Chaotic-avoiding trajectory's scheme for deterministic generation of single cavity solitons remains effective with the inclusion of thermal effects.

B. Deterministic SCS Generation

Generally, with the forward detuning procedure, the pump frequency is typically scanned from a blue-detuned to a red-detuned state. The evolution of the intracavity optical frequency comb is similar to the stages depicted in Fig. 4(d). However, the final result is the formation of multiple solitons with random quantities and positions, and the spectral lines of the optical frequency comb are not smooth. Through simulation, we obtained the distribution regions of different types of optical combs in the $(\alpha, |F|^2)$ parameter space (Fig. 5(a) and (b)). Here, we define a path that can access deterministic solitons under thermal effects (Fig. 5(a)). At the same time, this path also avoids the chaotic state experienced during the soliton evolution process. Due to the inclusion of thermal effects, we refer to this path as the "chaos-avoiding path under thermal effects (TCAT)":

$$F = -0.03778 + 0.05391 \quad *\exp \quad (43.01216 * \alpha). \tag{34}$$

The path is fitted with an exponential curve. To verify the feasibility of the chosen path, we linearly swept the frequency detuning from zero to a certain point at a constant rate and varied the input power based on the TCAT path in (34). Then, we kept

the detuning and pump power fixed for a period of time. Ultimately, depending on the different paths selected, we obtained the stable soliton states. It can be seen in Fig. 6 that the simulated results obtained in the end correspond to either a multi-soliton state or a single-soliton state optical comb. From the evolution graph, it is also observed that the evolution process of the soliton avoids chaotic states and unstable cavity soliton stages, directly reaching the stable cavity soliton stage. On one hand, by setting different starting points, various paths can be defined in the SMI and SCS regions (Fig. 5(a)), and the desired stable soliton comb can also be obtained. On the other hand, by setting different endpoints (in the SCS region), a single soliton state or multiple soliton states can be switched using the same determined path, as shown in Fig. 6. Fig. 6(a)–(c) depict the generation path (line A) of deterministic single solitons. Along this path, single solitons can be deterministically generated, and the evolution process of the comb clearly avoids chaotic states. Additionally, on the same deterministic path, different end points correspond to different results in the soliton evolution, that is, the number of solitons obtained is different. As shown in Fig. 6(d)–(f), when we start at the same point in parameter space but end in a different point, the corresponding result in a final state becomes a two-soliton comb. In addition, we also investigate the influence of different paths on the resulting solitons (Fig. 6(e)–(i)). When choosing path B, the comb eventually evolves into a multi-soliton state, but during the evolution process, it transitions from eight solitons initially to three solitons in the end. Hence, as long as the chosen paths only pass through Turing states and stable cavity soliton states, a deterministic soliton state can be obtained in the end.

V. Conclusion

In conclusion, we conduct a detailed study on the bifurcation analysis of the optical frequency comb and investigate the thermal-optical dynamic stability and spatial bifurcation problem of the optical frequency comb using the thermal LL equation. The influence of thermal effects on modulation instability (HH bifurcation) is investigated. The results show that thermal effects can affect the stability of microresonator frequency combs, the HH bifurcation in the bistable curve will transform into the BD bifurcation, resulting in the disappearance of modulation instability. In addition, we found that the thermal effect can increase the range of existence of solitons and improve its stability. Besides, we propose a method to obtain stable soliton states in a deterministic way under thermal effects by simultaneously tuning the cavity detuning and pump power. The deterministic access path of solitons must start with a relatively small detuning, because the resulting Turing rings in the case of small detuning have low intensity noise and high stability, making the Turing ring a good choice as our starting point. These soliton states can be multi-soliton states or single soliton states depending on the endpoint and the evolution process avoids the unstable chaotic states. The simulation results presented in this paper contribute to the practical application of microresonators as high-coherence and stable Kerr microcomb sources.

References

[1] J. Zheng et al., "Optical ranging system based on multiple pulse train interference using soliton microcomb," *Appl. Phys. Lett.*, vol. 118, no. 26, Jun. 2021, Art. no. 261106.

[2] L. Jia et al., "Nonlinear calibration of frequency modulated continuous wave LIDAR based on a microresonator soliton comb," *Opt. Lett.*, vol. 46, no. 5, pp. 1025–1028, Mar. 2021.

[3] J. Wang et al., "Long-distance ranging with high precision using a soliton microcomb," *Photon. Res.*, vol. 8, no. 12, pp. 1964–1974, Dec. 2020.

[4] R. A. Probst et al., "A crucial test for astronomical spectrograph calibration with frequency combs," *Nature Astron.*, vol. 4, no. 6, pp. 603–608, Feb. 2020.

[5] M. Tan et al., "Photonic RF arbitrary waveform generator based on a soliton crystal micro-comb source," *J. Lightw. Technol.*, vol. 38, no. 22, pp. 6221–6226, Nov. 2020.

[6] X. Xu et al., "Advanced RF and microwave functions based on an integrated optical frequency comb source," *Opt. Exp.*, vol. 26, no. 3, pp. 2569–2583, Feb. 2018.

[7] J. N. Kemal et al., "Multi-wavelength coherent transmission using an optical frequency comb as a local oscillator," *Opt. Exp.*, vol. 24, no. 22, pp. 25432–25445, Oct. 2016.

[8] J. Li et al., "All-optical synchronization of remote optomechanical systems," *Phys. Rev. Lett.*, vol. 129, no. 6, Aug. 2022, Art. no. 063605.

[9] Y. K. Chembo and C. R. Menyuk, "Spatiotemporal Lugiato-Lefever formalism for Kerr-comb generation in whispering-gallery-mode resonators," *Phys. Rev. A*, vol. 87, 2013, Art. no. 053852.

[10] L. A. Lugiato and R. Lefever, "Spatial dissipative structures in passive optical systems," *Phys. Rev. Lett.*, vol. 58, no. 21, pp. 2209–2211, May 1987.

[11] C. M. Arabí, P. Parra-Rivas, T. Hansson, L. Gelens, S. Wabnitz, and F. Leo, "Localized structures formed through domain wall locking in cavity-enhanced second-harmonic generation," *Opt. Lett.*, vol. 45, no. 20, pp. 5856–5859, Oct. 2020.

[12] P. Parra-Rivas et al., "Quartic Kerr cavity combs: Bright and dark solitons," *Opt. Lett.*, vol. 47, no. 10, pp. 2438–2441, May 2022.

[13] R. D. Dikandé Bitha and A. M. Dikandé, "Soliton-comb structures in ring-shaped optical microresonators: Generation, reconstruction and stability," *Eur. Phys. J. D*, vol. 73, no. 7, p. 152, Jul. 2019.

[14] R. D. Dikandé Bitha and A. M. Dikandé, "Elliptic-type soliton combs in optical ring microresonators," *Phys. Rev. A*, vol. 97, no. 3, Mar. 2018, Art. no. 033813.

[15] P. Parra-Rivas, E. Knobloch, L. Gelens, and D. Gomila, "Origin, bifurcation structure and stability of localized states in Kerr dispersive optical cavities," *IMA J. Appl. Math.*, vol. 86, no. 5, pp. 856–895, Oct. 2021.

[16] P. Parra-Rivas, S. Coulibaly, M. G. Clerc, and M. Tlidi, "Influence of stimulated Raman scattering on Kerr domain walls and localized structures," *Phys. Rev. A*, vol. 103, no. 1, Jan. 2021, Art. no. 013507.

[17] P. Parra-Rivas, D. Gomila, L. Gelens, and E. Knobloch, "Bifurcation structure of localized states in the Lugiato-Lefever equation with anomalous dispersion," *Phys. Rev. E*, vol. 97, no. 4, Apr. 2018, Art. no. 042204.

[18] P. Parra-Rivas, C. M. Arabí, and F. Leo, "Dissipative localized states and breathers in phase-mismatched singly resonant optical parametric oscillators: Bifurcation structure and stability," *Phys. Rev. Res.*, vol. 4, no. 1, Jan. 2022, Art. no. 013044.

[19] B. A. B. Cho, I. N. Ngek, and A. M. Dikandé, "Soliton crystals in optical Kerr microresonators in the presence of thermo-optic effects," *J. Opt.*, vol. 24, no. 11, Nov. 2022, Art. no. 115501.

[20] X. Xue et al., "Thermal tuning of Kerr frequency combs in silicon nitride microring resonators," *Opt. Exp.*, vol. 24, no. 1, pp. 687–698, Jan. 2016.

[21] C. Joshi et al., "Thermally controlled comb generation and soliton modelocking in microresonators," *Opt. Lett.*, vol. 41, no. 11, pp. 2565–2568, Jun. 2016.

[22] P. Del'Haye, K. Beha, S. B. Papp, and S. A. Diddams, "Self-injection locking and phase-locked states in microresonator-based optical frequency combs," *Phys. Rev. Lett.*, vol. 112, no. 4, Jan. 2014, Art. no. 043905.

[23] Z. Qi et al., "Deterministic access of broadband frequency combs in microresonators using cnoidal waves in the soliton crystal limit," *Opt. Exp.*, vol. 28, no. 24, Nov. 2020, Art. no. 36304.

[24] J. A. Jaramillo-Villegas, X. Xue, P.-H. Wang, D. E. Leaird, and A. M. Weiner, "Deterministic single soliton generation and compression in microring resonators avoiding the chaotic region," *Opt. Exp.*, vol. 23, no. 8, pp. 9618–9626, Apr. 2015.

[25] H. Zhou et al., "Soliton bursts and deterministic dissipative Kerr soliton generation in auxiliary-assisted microcavities," *Light: Sci. Appl.*, vol. 8, no. 1, May 2019, Art. no. 50.

[26] Z. Kang et al., "Deterministic generation of single soliton Kerr frequency comb in microresonators by a single shot pulsed trigger," *Opt. Exp.*, vol. 26, no. 14, pp. 18563–18577, Jul. 2018.
[27] H. Guo et al., "Universal dynamics and deterministic switching of dissipative Kerr solitons in optical microresonators," *Nature Phys.*, vol. 13, no. 1, pp. 94–102, 2017.
[28] M. R. E. Lamont, Y. Okawachi, and A. L. Gaeta, "Route to stabilized ultrabroadband microresonator-based frequency combs," *Opt. Lett.*, vol. 38, no. 18, pp. 3478–3481, Sep. 2013.
[29] Q. Li et al., "Stably accessing octave-spanning microresonator frequency combs in the soliton regime," *Optica*, vol. 4, no. 2, pp. 193–203, Feb. 2017.
[30] T. Wildi, V. Brasch, J. Liu, T. J. Kippenberg, and T. Herr, "Thermally stable access to microresonator solitons via slow pump modulation," *Opt. Lett.*, vol. 44, no. 18, pp. 4447–4450, Sep. 2019.
[31] H. Nejadriahi, A. Friedman, R. Sharma, S. Pappert, Y. Fainman, and P. Yu, "Thermo-optic properties of silicon-rich silicon nitride for on-chip applications," *Opt. Exp.*, vol. 28, no. 17, pp. 24951–24960, Aug. 2020.
[32] A. Leshem, Z. Qi, T. F. Carruthers, C. R. Menyuk, and O. Gat, "Thermal instabilities, frequency-comb formation, and temporal oscillations in Kerr microresonators," *Phys. Rev. A*, vol. 103, no. 1, Jan. 2021, Art. no. 013512.
[33] P. Parra-Rivas, E. Knobloch, D. Gomila, and L. Gelens, "Dark solitons in the Lugiato-Lefever equation with normal dispersion," *Phys. Rev. A*, vol. 93, no. 6, Jun. 2016, Art. no. 063839.
[34] P. Colet, M. A. Matías, L. Gelens, and D. Gomila, "Formation of localized structures in bistable systems through nonlocal spatial coupling. I. General framework," *Phys. Rev. E*, vol. 89, no. 1, Jan. 2014, Art. no. 012914.
[35] C. Godey, I. V. Balakireva, A. Coillet, and Y. K. Chembo, "Stability analysis of the spatiotemporal Lugiato-Lefever model for Kerr optical frequency combs in the anomalous and normal dispersion regimes," *Phys. Rev. A*, vol. 89, no. 6, Jun. 2014, Art. no. 063814.
[36] A. Coillet et al., "Azimuthal Turing patterns, bright and dark cavity solitons in Kerr combs generated with whispering-gallery-mode resonators," *IEEE Photon. J.*, vol. 5, no. 4, Aug. 2013, Art. no. 6100409.
[37] J. A. Jaramillo-Villegas et al., "Towards automated deterministic comb generation in microresonators: Overcoming thermal shift," in *Proc. Front. Opt.*, 2015, Paper FM2D.3.
[38] P. Parra-Rivas, D. Gomila, M. A. Matías, S. Coen, and L. Gelens, "Dynamics of localized and patterned structures in the Lugiato-Lefever equation determine the stability and shape of optical frequency combs," *Phys. Rev. A*, vol. 89, no. 4, Apr. 2014, Art. no. 043813.
[39] S. Coen and M. Erkintalo, "Universal scaling laws of Kerr frequency combs," *Opt. Lett.*, vol. 38, no. 11, pp. 1790–1792, Jun. 2013.